

ARTICLE

<https://doi.org/10.1038/s43246-020-00115-w>

OPEN



Emergent flat band electronic structure in a VSe₂/Bi₂Se₃ heterostructure

Turgut Yilmaz¹✉, Xiao Tong², Zhongwei Dai¹✉, Jerzy T. Sadowski¹✉, Eike F. Schwier³, Kenya Shimada¹✉, Sooyeon Hwang², Kim Kisslinger², Konstantine Kaznatcheev¹, Elio Vescovo¹ & Boris Sinkovic⁴

Flat band electronic states are proposed to be a fundamental tool to achieve various quantum states of matter at higher temperatures due to the enhanced electronic correlations. However, materials with such peculiar electronic states are rare and often rely on subtle properties of the band structures. Here, by using angle-resolved photoemission spectroscopy, we show the emergent flat band in a VSe₂ / Bi₂Se₃ heterostructure. Our photoemission study demonstrates that the flat band covers the entire Brillouin zone and exhibits 2D nature with a complex circular dichroism. In addition, the Dirac cone of Bi₂Se₃ is not reshaped by the flat band even though they overlap in proximity of the Dirac point. These features make this flat band distinguishable from the ones previously found. Thereby, the observation of a flat band in the VSe₂ / Bi₂Se₃ heterostructure opens a promising pathway to realize strongly correlated quantum effects in topological materials.

¹ National Synchrotron Light Source II, Brookhaven National Lab, Upton, New York 11973, USA. ² Center for Functional Nanomaterials, Brookhaven National Lab, Upton, New York 11973, USA. ³ Hiroshima Synchrotron Radiation Center, Hiroshima University, 2-313 Kagamiyama, Higashi Hiroshima 739-0046, Japan. ⁴ Department of Physics, University of Connecticut, Storrs, Connecticut 06269, USA. ✉email: tyilmaz@bnl.gov

The physics of solids is largely determined by their energy band structures. Therefore, the investigation and control of distinct electronic band dispersions assume a great length to understand and discover new states of the matter. One of the exotic electronic states is a type of flat band, which is predicted to host high-temperature superconductivity^{1–4}, fractional quantum Hall effect^{5,6}, and ferromagnetism^{7–9}. In superconductors, a flat band can boost the coupling constant and the transition temperature (T_c) as a result of an enhanced density of states at the Fermi level (E_F)^{10,11}. This mechanism was utilized to explain the unexpected superconductivity in rhombohedral graphite and twisted graphene^{12–14}. Other examples of flat band materials are Kagome lattices in which the flat band stems from destructive quantum interference due to the frustrated lattice geometry^{7,8}. The Kagome-type flat bands have been observed in FeSn and Fe₃Sn₂ by angle-resolved photoemission spectroscopy (ARPES) and in Co₃Sn₂S₂ by scanning tunneling spectroscopy (STS)^{8–10}. However, the complexity of the electronic structure in the photoemission data and the lack of momentum resolution in STS make the observations elusive. Computational efforts have also been made focusing on designing flat band transition metal dichalcogenides (TMDs) through the formation of the Moiré superlattices, which could support strongly correlated physics at higher temperatures^{15–17}. All these previous works conclude that the flat band media could be fertile to many novel states of the matter. However, the limited number of the materials with such non-trivial bands hinders future studies.

Motivated by earlier studies, we investigate the surface electronic structure of VSe₂ TMD grown on the surface of Bi₂Se₃ topological insulator (TI) and show the emergence of a flat band in the electronic states. This flat band covers the entire k_x - k_y plane of the Brillouin zone (BZ) and displays dispersionless behavior along the k_z direction as well. Furthermore, circular dichroism ARPES (CD-ARPES) measurements reveal that the CD signal of the flat band reverses the sign at several points within the BZ. Another notable observation is that the VSe₂ overlayer and the emergence of the flat band do not reshape the Dirac cone of Bi₂Se₃ in the vicinity of the Dirac point (DP) unlike the case of transition metal doping which opens a large gap at the DP¹⁸. We also observe Moiré patterns in VSe₂ domains of monolayer (ML) thickness and stripe-type patterns in bare Bi₂Se₃ through scanning tunneling microscopy (STM). Further elucidations on the crystalline and chemical properties of the system are provided by scanning transmission electron microscopy (STEM), and micro-spot low-energy electron diffraction (μ LEED). Our results demonstrate a rich physics in this system and suggest a large family of materials as possible emergent flat bands and thus will motivate future studies based on heterostructure formed by other quantum materials such as superconductors.

Results

Structural properties. Bi₂Se₃ and VSe₂ are layered materials with their atomic stacking geometry shown in Fig. 1a. The layers in each compound are separated by van der Waals (vdW) gaps with weak covalent out-of-plane bonds connecting the layers. These properties allow for the formation of well-ordered VSe₂/Bi₂Se₃ heterostructure despite the large in-plane lattice mismatch of around 20% between the two materials^{19,20}. Figure 1b, c depict the relevant core-levels of such structures 0 ML, 0.3 ML, 2 ML, and 3 ML VSe₂ on 12 quintuple layer (QL) Bi₂Se₃. Upon deposition of the VSe₂, the Bi 5d peaks of Bi₂Se₃ located at 25.1 and 28 eV remain at the same binding energies, indicating the absence of V metals at the interface and/or in the bulk (Fig. 1b)²¹. This also shows that VSe₂ surface deposition does not modify the chemical potential of Bi₂Se₃ seen as the absence of an electron or

hole doping effect. Compared with pristine Bi₂Se₃, the Se 3d peak, however, appears at 0.1 eV higher binding energy for VSe₂ grown sample. The difference in binding energy is possibly related to the charge density wave (CDW) phase of VSe₂¹⁹. Furthermore, V 2p_{1/2} and 2p_{3/2} peaks of VSe₂ shown in Fig. 1c are located at 513 and 520.6 eV binding energies corresponding to +4 oxidation states being in agreement with the recent report²⁰.

To further explore the system, we show a high-angle annular dark-field (HAADF)-STEM cross-section image of a 3 ML VSe₂/12 QL Bi₂Se₃ heterostructure in Fig. 1d. Bi₂Se₃ and VSe₂ exhibit regular atomic layers with smooth interfaces and vdW gaps marked with red arrows in Fig. 1d. On the other hand, the interface spacing between the Bi₂Se₃ and VSe₂ layers comparably smaller than the vdW gaps which could strongly modify the local electronic structure. Furthermore, the STEM energy dispersive X-ray spectroscopy elemental maps presented in Supplementary Fig. 1 show the atomic distribution of Bi in the Bi₂Se₃ layers, V in VSe₂ layers, and Se across the heterostructure as expected.

To study the local crystal structure, Fig. 1e, f show the STM image of Bi₂Se₃ and VSe₂ regions of a 0.3 ML VSe₂/12 QL Bi₂Se₃ sample, respectively. The Bi₂Se₃ surface has a stripe-like pattern similar to Cs and Fe doped Bi₂Se₃²². The STM image of the VSe₂ domains presented in Fig. 1f exhibits a Moiré pattern with \sim 2 nm \times 2 nm superstructure. This differs from the previous studies conducted on VSe₂/graphene¹⁹. Moiré pattern can be formed by a small misfit between the in-plane lattice parameters of the film and the underlying material or the relative rotation of two layers to each other, or both. By contrast, the lattice mismatch between the VSe₂ and Bi₂Se₃ is quite large (about 20%). Unfortunately, we cannot make a quantitative analysis for precise determination of the in-plane lattice parameters or the atomic displacement due to the limitation in our STM data taken at room-temperature experiment. However, similar Moiré pattern formation is also observed on ML MoSe₂ grown on a graphene substrate whose origin is attributed to the lattice mismatch between the multiple unit cells of the two materials²³. Thereby, the Moiré pattern in VSe₂ could be formed due to the small mismatch between four–five-unit cells of Bi₂Se₃ ($4a_{BS} = 16.56$ Å or $5a_{BS} = 20.7$ Å) and five-unit cells of VSe₂ ($5a_{VS} = 16.8$ Å or $6a_{VS} = 20.16$ Å) for the rotationally aligned lattice geometry. Alternatively, the Moiré pattern could form be formed by the rotational misalignments of Bi₂Se₃ and VSe₂ atomic lattices. Moreover, the details of the STM data reveal that the layer height is 6.8 Å for VSe₂ (Supplementary Fig. 2) being in the line with the recent findings²⁴.

Observation of the flat band in a VSe₂/Bi₂Se₃ heterostructure.

To examine the band structure, the binding energy vs. k_x plots are given in Fig. 2a for 12 QL Bi₂Se₃ and in Fig. 2b–d for various thickness of VSe₂ on 12 QL Bi₂Se₃. Bi₂Se₃ exhibits the typical band structure with the linear Dirac surface states (DSSs) forming the Dirac cone with the Dirac point (DP) at 0.36 eV below E_F ²⁵. Upon deposition of 0.3 ML VSe₂ on the surface of Bi₂Se₃, a flat band at 0.47 eV binding energy and with a \sim 0.18 eV bandwidth emerges in the surface electronic structure (Fig. 2b). The flatness of the band is well distinguished in the ARPES maps where bulk bands and the DSS of Bi₂Se₃ strongly disperse as a function of k_x , while the flat band retains dispersionless across the $\bar{\Gamma} - \bar{M}$ high-symmetry lines. VSe₂ growth also induces the well-known M-state quantization²⁶ of the bulk valance band of Bi₂Se₃ shown in Fig. 2b. The flat band can be resolved in 1 ML and, less intense, in 2 ML VSe₂ (Fig. 2c, d) and further increasing the thickness of VSe₂ to 3 ML leads to disappearance of the flat band from the ARPES map (Fig. 2e). On the other side, the thicker VSe₂ grown on a Bi₂Se₃ exhibits the same electronic feature with the one grown on a highly ordered pyrolytic graphite (HOPG) substrate

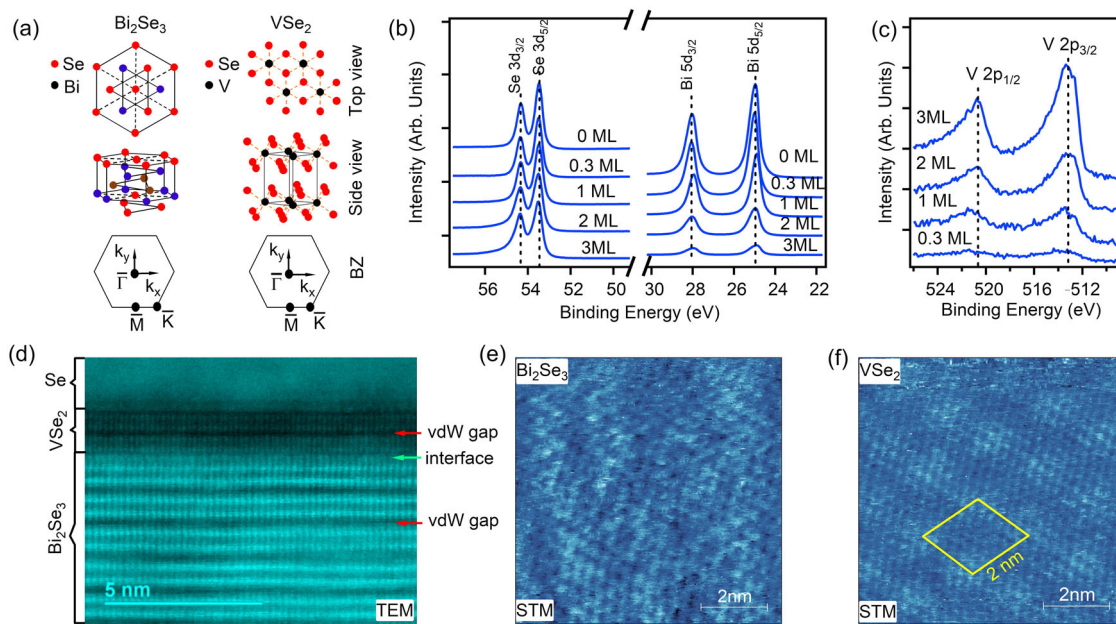


Fig. 1 Structural characterization of the VSe₂/Bi₂Se₃ heterostructures. **a** Schematic representations of the top and side views of Bi₂Se₃ and VSe₂ crystal structures. Hexagonal BZs with the high-symmetry points are given in the lower part of **a**. **b** Core-level photoemission spectra of Bi 5d and Se 3d of 0, 0.3, 1, 2, and 3 ML VSe₂/12 QL Bi₂Se₃ heterostructures. **c** V 2p core levels for 0.3, 1, 2, and 3 ML VSe₂/12 QL Bi₂Se₃ heterostructures. The atomic stoichiometry of Se to V is computed to be 2 by using the peak areas and photoionization cross-sections. Bi 5d and Se 3d peaks were recorded with 110 eV synchrotron radiation, whereas V 2p peaks were conducted by using 700 eV synchrotron radiation. **d** HAADF-STEM cross-section image of 3 ML VSe₂/12 QL Bi₂Se₃ heterostructure. The color contrast in **d** is correlated with the atomic number (Z-contrast). **e**, **f** Room-temperature STM images of Bi₂Se₃ (at sample bias 100 mV, set point 1 nA) and VSe₂ (at sample bias 80 mV, set point 1 nA) surfaces, respectively, obtained from 0.3 ML VSe₂/12 QL Bi₂Se₃. Yellow parallelogram in **f** represents the unit cell of Moiré pattern.

(Fig. 2f), indicating that the Bi₂Se₃ sublayer plays a crucial role in the formation of the new electronic states. It is also noticeable that the nature of the flat band stays unchanged with increasing VSe₂ thickness as its binding energy and dispersionless character remain the same. The only observable evolution is in the spectral intensity which gradually decreases with increasing VSe₂ thickness. This emphasized in Fig. 2g displaying the energy distribution curves (EDCs) taken at $k_x = -0.25 \text{ \AA}^{-1}$ from each ARPES maps. The peak stemming from the flat band can be seen up to 2 ML VSe₂, while it is not visible for thicker films. This is likely to be correlated with the electron mean free path and suggests that this state is localized at the interface between the two materials. This can be further confirmed by taking advantage of energy dependency of the electron mean free path. In Fig. 2h, the EDCs at $k_x = -0.3 \text{ \AA}^{-1}$ for a 3 ML VSe₂/12 QL Bi₂Se₃ heterostructure are shown for three photon energies. As expected, due to the enhanced electron mean free path²⁷, a shoulder on the high binding energy side of V 3d develops with increasing photon energy from 50 to 220 eV, supporting interface-induced flat band argument.

Another interesting observation is that the flat band overlaps with the lower branch of the Dirac cone in the vicinity of $k_x = 0 \text{ \AA}^{-1}$ without inducing any prominent change in its spectral shape. This can be even better seen in the films with the thicker VSe₂ coverage confirming that the flat band, DSSs, and the dispersive V 3d state of VSe₂ coexist in the surface electronic structure (Fig. 2b-d and Supplementary Fig. 5). It is also found that the DP of Bi₂Se₃ does not experience an energy shift upon surface deposition of VSe₂. This indicates the absence of any band bending effect which is consistent with the behavior of Bi 5d core levels presented in Fig. 1b.

To further investigate the flat band, a k_x - k_y intensity plots at E_F and at the binding energy of the flat band (E_{FB}) for a 1 ML VSe₂/12

QL Bi₂Se₃ sample are shown in Fig. 2i, j, respectively. The Fermi surface is dominated by a flower-like electron pocket formed by the V 3d orbitals of VSe₂ centered at $\bar{\Gamma}$ point as similar to the earlier observation for VSe₂ grown on different substrates²⁸. The constant energy cut at E_{FB} is instead quite featureless. Besides, a weak residual of the start-like features of VSe₂, no new, distinct dispersion is seen along the any direction of the BZ. This indicates that the flat band fills the entire BZs of Bi₂Se₃ and VSe₂ as depicted by blue and red hexagons in Fig. 2i, j, respectively. This can be also seen in Supplementary Fig. 4 where the spectra taken along the different directions in the BZ for fixed k_x and k_y momentum all show the existence of the flat band. Such electronic state spread over a large momentum area can significantly enhance the electronic correlation yielding quantum effects at very high-temperatures. It is also worth noting that the LEED pattern of the sample shows stretched diffraction spots along the rotational direction indicating the presence of the rotationally misaligned VSe₂ domains (Supplementary Fig. 2a) with respect to each other and to the Bi₂Se₃ substrate. The rotational misfit of $\pm 3^\circ$ estimated from μ LEED pattern, however, is too small for a band to span whole BZ and to induce a fully occupied constant energy counter in the momentum space.

In Fig. 2k, we also present an ARPES map covering two BZ centers. The flat band connects two $\bar{\Gamma}$ points to each other. Another intriguing realization in this spectra is that the Bi₂Se₃ and VSe₂ shares the same in-plane lattice constants. This is consistent with our LEED measurements, which does not show distinct diffraction patterns arising from VSe₂ and Bi₂Se₃ (Supplementary Fig. 2a). This is supported with the EDC taken at the Fermi level and given on the top of the spectra in Fig. 2k. Two zone centers are separated with $k_x = 1.9 \text{ \AA}^{-1}$ yielding a 4.03 \AA in-plane lattice parameter. This is smaller than in-lane lattice

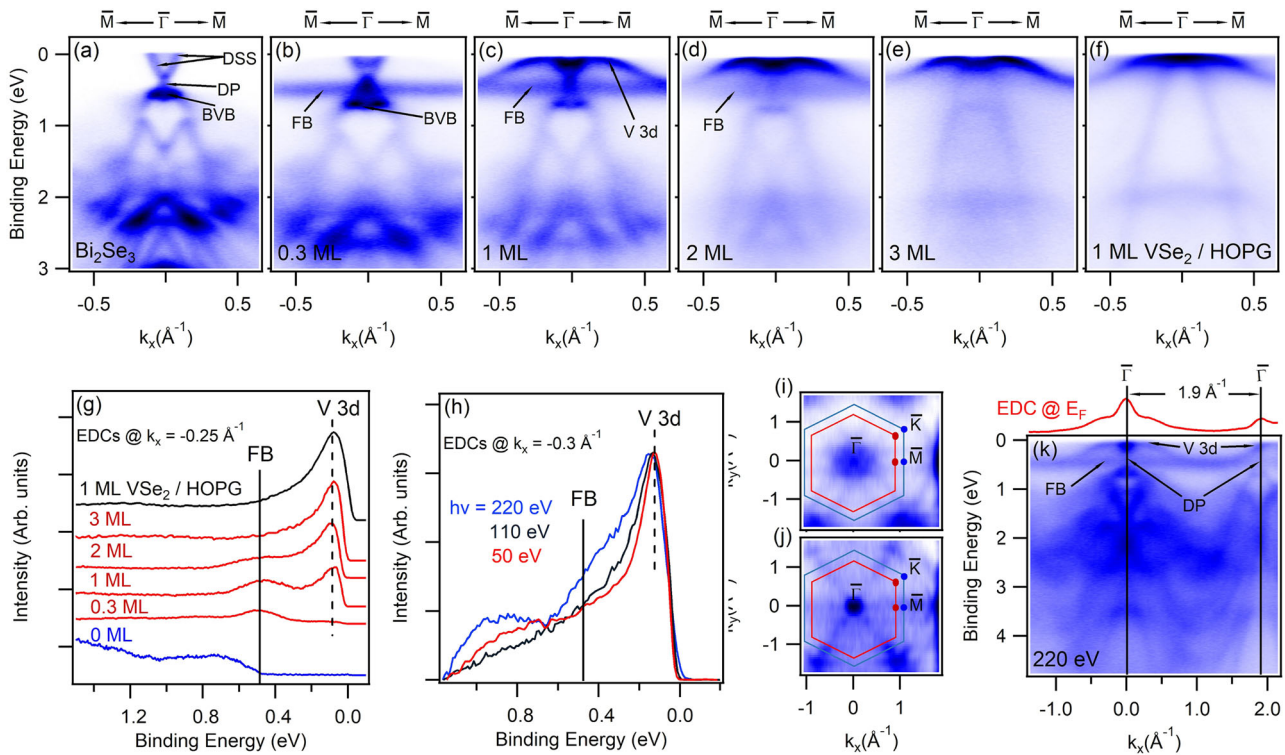


Fig. 2 Observation of the flat band in the VSe₂/Bi₂Se₃ heterostructures. **a** Experimental electronic structures of a 12 QL Bi₂Se₃ sample. **b–e** Electronic structure of 0.3, 1, 2, and 3 ML VSe₂/12 QL Bi₂Se₃ heterostructures, respectively. **f** Electronic structure of 1 ML VSe₂ grown on a HOPG substrate. Spectra in **a–f** were collected with 110 eV linear horizontal polarized lights along the $\bar{\Gamma} - \bar{M}$ direction in the BZ. BVB represents the bulk valence band of Bi₂Se₃. **g** Corresponding EDCs obtained along the $k_x = -0.25 \text{ \AA}^{-1}$. **h** Photon energy-dependent EDCs of 3 ML VSe₂/1/2 QL Bi₂Se₃ obtained with 50, 110, and 220 eV photons. A Tougaard background is subtracted from each spectrum. The corresponding ARPES maps are presented in Supplementary Fig. 3. **i, j** Constant energy counters at the E_F and the E_{FB} for 1 ML VSe₂/1/2 QL Bi₂Se₃ sample, respectively. The momentum maps were recorded with 169 eV photons and the corresponding ARPES map can be found in Supplementary Fig. 4. **k** Wide momentum window ARPES map of the 1 ML VSe₂/1/2 QL Bi₂Se₃ sample obtained with 220 eV photon energy along the $\bar{\Gamma} - \bar{M}$ direction of the BZ. The EDC on the top of **k** is obtained at the E_F . Blue and red hexagons in **i, j** correspond to the BZs of VSe₂ and Bi₂Se₃, respectively. In-plane lattice parameters of 4.14 \AA for Bi₂Se₃ and 3.356 \AA for VSe₂ were employed to compute the BZs^{27,31}.

parameter of Bi₂Se₃ ($a = 4.545 \text{ \AA}$)¹⁹, while larger than the one of VSe₂ ($a = 3.356 \text{ \AA}$)²³. This strong lattice relaxation can significantly modify the electronic structure of both material in the vicinity of the interface and induce new electronic states.

Photon energy-dependent electronic structure. In ARPES experiments, by recording the electronic structure with a wide photon energy range, a k_{\parallel} vs. k_z or binding energy vs. k_z dispersions can be also extracted. This method allows studying the dispersion of the energy bands along the k_z (out-of-plane) direction to distinguish the two-dimensional (2D) bands from the dispersive bulk bands. Such spectra acquired at varying photon energies (from 45 to 120 eV with 5 eV steps) for a 1 ML VSe₂/12 QL Bi₂Se₃ heterostructure are given in Fig. 3. In the plot of k_z vs. k_y dispersion at E_F , DSSs marked with dashed black lines exhibit no k_z dependence (Fig. 3a). Similar spectrum at E_{FB} given in Fig. 3b shows that a high spectral intensity along the $k_y = 0 \text{ \AA}^{-1}$ originates from the bottom of the Dirac cone of Bi₂Se₃. Away from the $k_y = 0 \text{ \AA}^{-1}$, the plot has non-vanishing spectral intensity contributed by the flat band. This can be better seen in the momentum distribution curves obtained at various k_z points (Fig. 3c) in which each spectrum exhibits always finite density of states along the k_y momentum direction. This implies the dispersionless nature of the flat band along the k_z momentum direction. To further validate this observation, we present the binding energy– k_z plots along the $k_y = \pm 0.25 \text{ \AA}^{-1}$ in Fig. 3d, e, respectively. The plots clearly show that the flat band at 0.47 eV

binding energy is k_z independent confirming its non-bulk derived nature. We should also note that the M-shape bulk band located in the vicinity of 1 eV binding energy exhibits a nearly non-dispersive feature along the k_z as shown in Fig. 3d, e. To further reveal the details of the flat band, Fig. 3f depicts the EDCs taken at different k_z points. One can see that the EDC of the flat band does not exhibit a k_z -dependent evolution in the binding energy and bandwidth, providing a signature that it has 2D nature and originates from single type of atomic orbital.

Circular dichroism ARPES. CD-ARPES has gained great attention due to its feasibility to investigate the helical spin-orbit texture in topological surface states²⁹. The principle of the method is the spectral weight differences in ARPES arising from the opposite helicity of the circularly polarized lights. CD-ARPES is then obtained from $[(I_{RCP} - I_{LCP})]/[(I_{RCP} + I_{LCP})]$ where I_{RCP} and I_{LCP} are photoemission intensities for right hand circular polarized (RCP) and left hand circular polarized (LCP) lights, respectively. Thus, we have recorded the band structure of 0.3 ML VSe₂/12 QL Bi₂Se₃ sample with RCP and LCP, shown in Fig. 4a, b, respectively. The corresponding CD-ARPES is presented in a binary color map in Fig. 4c (red: negative-CD and blue: positive-CD). The bulk bands of Bi₂Se₃ dispersing below 0.8 eV binding energy show a strong CD signal as seen in Fig. 4a–c. CD signal of the DSSs exhibits a spectral weight switching from the $-k_y$ to $+k_y$ regions when changing the excitation energy from RCP to LCP. For clarity, the DC signal vs. k_y is plotted in Fig. 4d at 0.1 eV

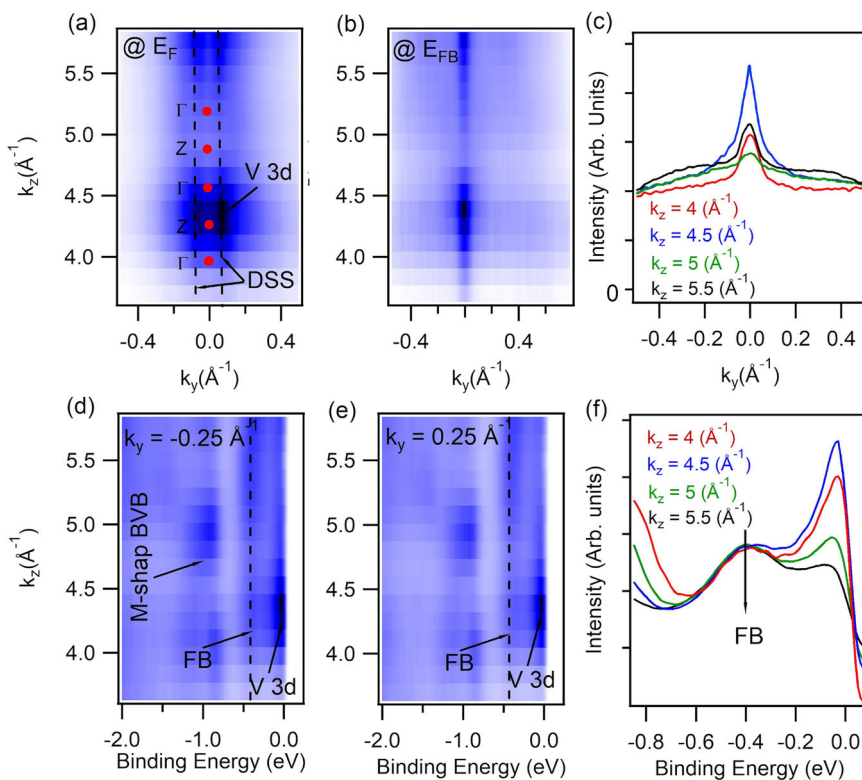


Fig. 3 Photon energy-dependent electronic structure of a 1ML VSe₂/12QL Bi₂Se₃ heterostructure. **a, b** k_y - k_z dispersions at the E_F and the E_{FB} , respectively. Dashed red lines in **a** mark the DSSs. **c** MDCs at different k_z points. **d, e** Binding energy vs. k_z maps at $k_y = \pm 0.25 \text{ \AA}^{-1}$, respectively. Dashed cyan colored lines in **d** and **e** represent the dispersion of the flat band along the k_z direction. **f** EDCs at various k_z points to study the spectral shape of the flat band. ARPES maps for the plots were conducted along the $\bar{\Gamma} - \bar{K}$ direction in the BZ. Data were conducted from the 1ML VSe₂/12QL Bi₂Se₃ heterostructure at 10 K.

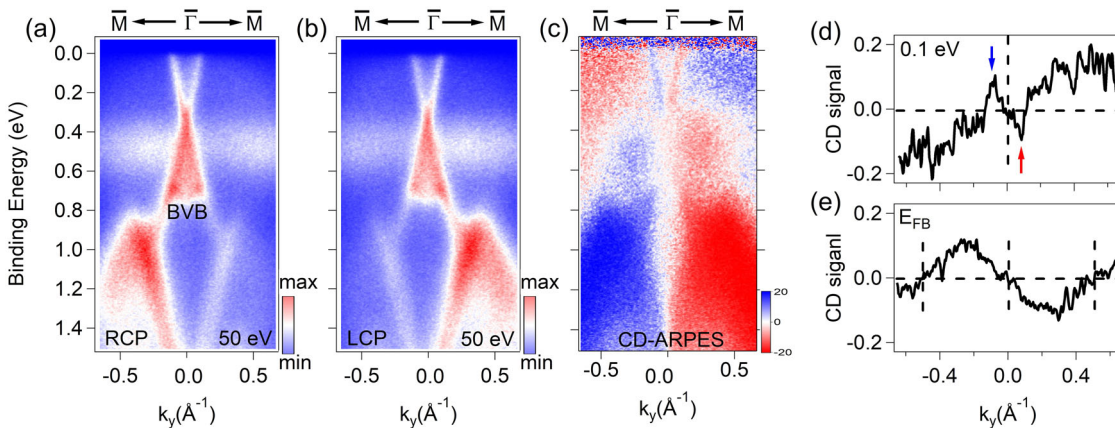


Fig. 4 CD-ARPES. **a, b** ARPES maps of 0.3ML VSe₂/12QL Bi₂Se₃ sample recorded with RCP and LCP lights, respectively. **c** Computed CD-ARPES. **d, e** CDs as a function of k_y at 0.1 eV binding energy and the E_{FB} , respectively.

binding energy where the CD is positive for left and negative for the right side of the Dirac cone, marked with vertical arrows. Further away from the $k_y = 0 \text{ \AA}^{-1}$, the plot in Fig. 4d still shows non-zero CD. This is likely originating from the V 3d orbitals, which dominate the density of states at the E_F for VSe₂¹⁹.

To investigate the dichroism effect in the flat band, the CD at E_{FB} is also plotted as a function of k_y in Fig. 4e and it exhibits sign inversions at $k_y = 0 \text{ \AA}^{-1}$ and $k_y = \pm 0.5 \text{ \AA}^{-1}$, and the maxima at $k_y = \pm 0.25 \text{ \AA}^{-1}$. This shows that similar to the DSSs, the CD in the flat band also exhibits helical texture where opposite k_y momenta have opposite signs of the CD. Notably, zero CD signal is also observed as white color in the CD-ARPES along the

$k_y = 0 \text{ \AA}^{-1}$. This depicts the nodal line, which was proposed to be the characteristic feature of the 2D electronic structure³⁰. In particular, the CD signal of the DSSs depends on the incident photon energy assigning it to the final state effect in the photoemission process²⁹. This was discussed in ref. ³⁰ with details where they propose the non-trivial connection between the spin-orbit texture and the CD signal. Thereby, the helical CD texture and the nodal line band suggest that the flat band could be topologically non-trivial.

Temperature-dependent electronic structure. To further study the nature of the flat band in detail, we present the temperature-

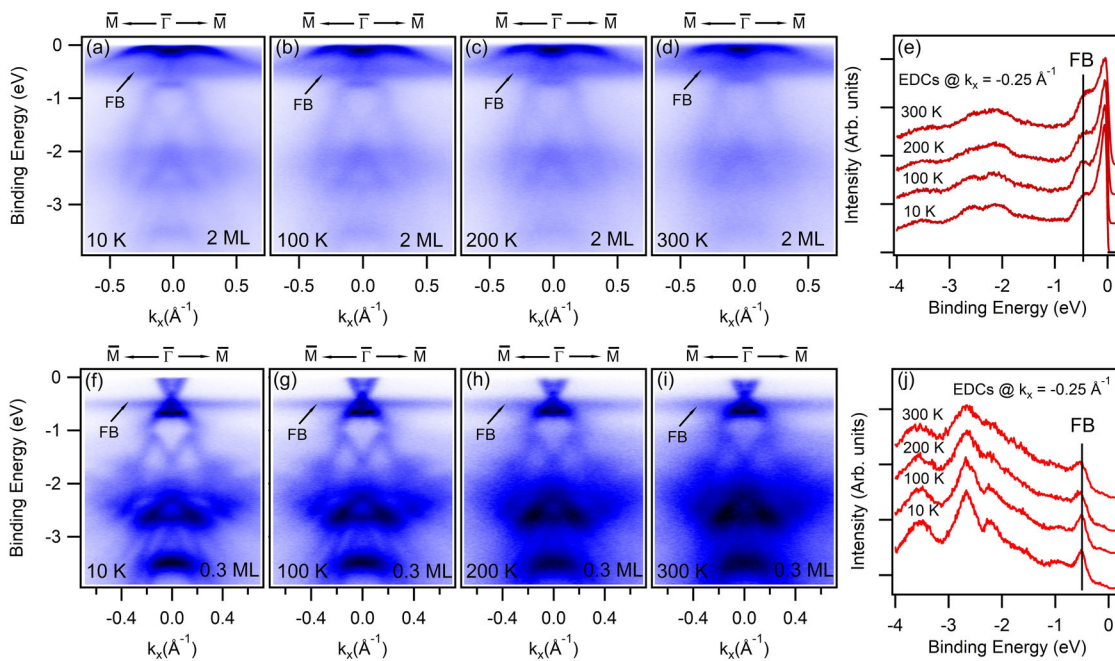


Fig. 5 Temperature-dependent electronic structure of the VSe₂/Bi₂Se₃ heterostructures. a-d ARPES maps of 2 ML VSe₂/12 QL Bi₂Se₃ at 10, 100, 200, and 300 K, respectively. **e** EDCs obtained along the $k_y = -0.25 \text{ \AA}^{-1}$ from each spectrum. **f-j** Same as a-e but for 0.3 ML VSe₂/12 QL Bi₂Se₃ sample. Spectra were obtained with 110 eV photons.

dependent ARPES maps of 1 ML VSe₂/12 QL Bi₂Se₃ in Fig. 5a-d and 0.3 ML VSe₂/12 QL Bi₂Se₃ in Fig. 5f-j for 10, 100, 200, and 300 K, respectively. For both samples, the temperature does not induce a prominent change on the nondispersive nature of the flat. This can be seen in the EDCs obtained along the $k_y = -0.25 \text{ \AA}^{-1}$ from the ARPES maps (Fig. 5e-j). It is clear from the data that temperature does not affect the line shape or the binding energy of the flat band. At any given temperature, the flat band is located at 0.47 eV. Only noticeable change is the broadening of all spectral features with increasing temperature as can be expected from phonon contributions to the total lifetime. On the other side, these data constitute a strong indication that the flat band is not likely to originate from disorder or impurities. The disorder usually shows a considerable dependence on the temperature as a modulation in the density of defects. This refers that the binding energy and the density of the states of the flat band should change if it is formed by the impurities or disorders. This can be found in a recent study where the disorder induced kink like states in Bi₂Se₃ can be diminished by lightly annealing the sample³¹. The temperature-dependent ARPES data also show that the flat band is not due to surface impurities. It is expected that the impurities will segregate into the bulk of Bi₂Se₃ and locate in sublattices with increasing temperature³². This will significantly modify the chemical potential of the system. A number of ARPES studies have been devoted to studying the effects of the adatoms on the band structure of Bi₂Se₃ and the only change found has been electron or hole doping^{18,26,32}. No experimental work has shown indication of any new states or flat like bands induced by surface impurities on the surface electronic structure of a TI. Furthermore, resonant ARPES experiments also revealed that the transition metal impurity states evolve onto the surface states rather than forming a flat band^{33,34}. Finally, it is worth mentioning that the ARPES maps taken at room temperature can be compared with the room-temperature STM data presented in Fig. 1f, leading to the conclusion that the Moiré pattern and the flat band electronic states coexist in our system.

Discussion

Here we present a detailed ARPES study on a VSe₂/Bi₂Se₃ system and showed unexpected formation of a flat band on the surface electronic structure on this heterostructure. One of the first scenario to consider as the origin of the flat band is the surface V impurities. Even though the theory predicts nearly nondispersive features induced by impurities or disorders in TIs^{31,35}, experimental studies shows that these states evolve onto the surface states rather than being flat in the momentum space^{33,34}. Also, in contrast to our results, these states are expected to strongly modify the Dirac cone and open an energy gap at the DP^{31,35}. Another scenario to consider would be the existence of superlattices as seen in $\sqrt{3} \times \sqrt{3}$ silicene superstructure by STS where the local density of states forms the electronic Kagome lattice³⁶. Interface dislocation or strain can also flatten the original bands by introducing pseudo-magnetic field term to the Hamiltonian in Moiré superstructures⁴. Furthermore, a pronounced band flattening in this scenario requires superstructure patterns with at least a few tens of nanometers periodicity which is much larger than one observed in the present case. However, in contrast to our observations, the flat band discussed within the superlattice frameworks is dispersionless only in the BZ of the superstructure^{17,36}.

On the other hand, our results show the emergent character of our flat band, which is likely due to the formation of the interface in the heterostructure between Bi₂Se₃ sublayer and VSe₂ top layer. This conclusion is supported by thickness and photon energy-dependent photoemission data showing that the flat band can be resolved with higher photon energies on thicker VSe₂ films. As a first example of the dispersionless electronic excitation in a topologically non-trivial band structure, our results could open a new pathway in the critical field of experimental realization and control of novel quantum effects.

Methods

Synthesis. Molecular beam epitaxial growth (MBE) technique was employed to grow VSe₂/Bi₂Se₃ and Bi₂Se₃ samples in a custom ultrahigh vacuum system located at the ESM beamline of NSLS-II. Se and Bi sources (5 N) were evaporated from the

ceramic crucibles while the e-beam evaporation method was used for V (99.8% purity) source. All samples were grown on Al_2O_3 (0001) substrates at 255 °C. Before the growth, the substrates were first degassed at 550 °C for three hours and flashed at 850 °C for 5 min. An ML VSe₂ were grown on a freshly cleaved HOPG substrate at 255 °C after annealing the substrate at 350 °C for 2 h. Sample thicknesses were estimated within a 15% error bar by using a quartz thickness monitor and X-ray photoemission spectroscopy. Samples for ARPES and μ LEED experiments were capped with 20 nm amorphous Se film before being removed from the MBE chamber.

Core-level spectroscopy. Core-levels were recorded at 21-ID-1 ESM beamline of National Synchrotron Light Source II (NSLS-II) by using a DA30 Scienta electron spectrometer at 10 K sample temperature.

Angle-resolved photoemission spectroscopy. ARPES experiments were performed at 21-ID-1 ESM beamline of NSLS-II by using a DA30 Scienta electron spectrometer. The pressure in the photoemission chamber was 1×10^{-10} Torr and samples were kept at 15 K during the experiment by a closed-cycle He cryostat. The energy resolution in the ARPES experiments was better than 15 meV with a spot size of $\sim 20 \mu\text{m}$. Before the ARPES experiments, samples were annealed at 220 °C for 30 min to remove the Se capping layer. The angle between the light and the surface normal of the sample is 55° at the normal emission during the ARPES experiments. The films were grounded with a tantalum clip. A part of the ARPES experiments was conducted at the linear undulator beamline at the Hiroshima Synchrotron Radiation Center BL-1 (Supplementary Fig. 5). Photon energy is converted to k_z momentum space by using the free electron final state approximation $\hbar k_z = \sqrt{2m_e(E_{\text{kin}}\cos^2\theta + V_0)}$ where m_e is the free electron mass, E_{kin} is the kinetic energy of a photoelectron, and V_0 is the inner potential taken as 11.8 eV for Bi₂Se₃³⁷.

TEM and STM microscopy. HAADF-STEM images were acquired with Hitachi HD2700C dedicated STEM with a probe Cs corrector operating at 200 kV at room temperature. Samples were prepared using the in-situ lift-out method on the FEI Helios 600 Nanolab dual-beam FIB. Final milling was completed at 2 keV. STM (Omicron VT- STM -XA 650) experiments were performed in an ultrahigh vacuum (UHV) system with a base pressure of 2×10^{-10} Torr at room temperature. All the STM images were observed in constant current mode using Pt/Ir tips. All bias values in the text refer to the bias applied to the sample. The STM images were analyzed using Gwyddion-2.55 software package. HAADF-STEM and STM experiments were conducted at the Center for Functional Nanomaterials, Brookhaven National Laboratory. Samples for STM were transferred with a vacuum suitcase.

Low-energy electron diffraction. μ LEED experiment was performed at X-ray photoemission electron microscopy/low-energy electron microscopy (XPEEM/LEEM) endstation of the ESM beamline (21-ID-2).

Data availability

The data that support the findings of this study are available from the corresponding author upon request.

Received: 25 November 2020; Accepted: 12 December 2020;

Published online: 20 January 2021

References

- Heikkilä, T. & Volovik, G. E. *Flat Bands as a Route to High-Temperature Superconductivity in Graphite* (ed. Esquinazi, P.) 123–144 (Springer, Switzerland, 2016).
- Cao, Y. et al. Unconventional superconductivity in magic-angle graphene superlattices. *Nature* **556**, 43–50 (2018).
- Heikkilä, T. T., Kopnin, N. B. & Volovik, G. E. Flat bands in topological media. *JETP Lett.* **94**, 233–239 (2011).
- Tang, E. & Fu, L. Strain-induced partially flat band, helical snake states and interface superconductivity in topological crystalline insulators. *Nat. Phys.* **10**, 964969 (2014).
- Tang, E., Mei, J. W. & Wen, X. G. High-temperature fractional quantum Hall states. *Phys. Rev. Lett.* **106**, 236802 (2011).
- Sun, K., Gu, Z., Katsura, H. & Das Sarma, S. Nearly flatbands with nontrivial topology. *Phys. Rev. Lett.* **106**, 236803 (2011).
- Guo, H. M. & Franz, M. Topological insulator on the kagome lattice. *Phys. Rev. B* **80**, 113102 (2009).
- Lin, Z. et al. Flatbands and emergent ferromagnetic ordering in Fe₃Sn₂ kagome lattices. *Phys. Rev. Lett.* **121**, 96401 (2018).
- Kang, M. et al. Dirac fermions and flat bands in the ideal Kagome metal FeSn. *Nat. Mater.* **19**, 163–169 (2020).
- Yin, J. X. et al. Negative flat band magnetism in a spin-orbit-coupled correlated kagome magnet. *Nat. Phys.* **15**, 443–448 (2019).
- Kopnin, N. B., Heikkilä, T. T. & Volovik, G. E. High-temperature surface superconductivity in topological flat-band systems. *Phys. Rev. B* **83**, 220503(R) (2011).
- Kopnin, N. B., Ijäs, M., Harju, A. & Heikkilä, T. T. High-temperature surface superconductivity in rhombohedral graphite. *Phys. Rev. B* **87**, 140503 (2013).
- Marchenko, D. et al. Extremely flat band in bilayer graphene. *Sci. Adv.* **4**, 11 (2018).
- Volovik, G. E. Graphite, graphene and the flat band superconductivity. *JETP Lett.* **107**, 516–517 (2018).
- Wu, F., Lovorn, T., Tutuc, E. & MacDonald, A. H. Hubbard model physics in transition metal dichalcogenide moiré bands. *Phys. Rev. Lett.* **121**, 026402 (2018).
- Naik, M. H. & Jain, M. Ultraflatbands and shear solitons in moiré patterns of twisted bilayer transition metal dichalcogenides. *Phys. Rev. Lett.* **121**, 266401 (2018).
- Bi, Z., Yuan, N. F. Q. & Fu, L. Designing flat bands by strain. *Phys. Rev. B* **100**, 035448 (2019).
- Yilmaz, T. et al. Distinct effects of Cr bulk doping and surface deposition on the chemical environment and electronic structure of the topological insulator Bi₂Se₃. *Appl. Surf. Sci.* **407**, 371–378 (2017).
- Chen, P. et al. Unique gap structure and symmetry of the charge density wave in single-layer VSe₂. *Phys. Rev. Lett.* **121**, 196402 (2018).
- Liu, Z. L. et al. Epitaxially grown monolayer VSe₂: an air-stable magnetic two-dimensional material with low work function at edges. *Sci. Bull.* **63**, 419 (2018).
- Walsh, L. A. et al. Interface chemistry of contact metals and ferromagnets on the topological insulator Bi₂Se₃. *J. Phys. Chem. C* **121**, 23551 (2017).
- Shokri, R. Coexistence of impurity-induced quasi-one-dimensional electronic structure and topological surface states of Bi₂Se₃. *J. Appl. Phys.* **119**, 085304 (2016).
- Ugeda, M. M. et al. Giant bandgap renormalization and excitonic effects in a monolayer transition metal dichalcogenide semiconductor. *Nat. Mater.* **13**, 1091–1095 (2014).
- Duvjir, G. et al. Emergence of a metal-insulator transition and high-temperature charge-density waves in VSe₂ at the monolayer limit. *Nano Lett.* **18**, 5432–5438 (2018).
- Xia, Y. et al. Observation of a large-gap topological-insulator class with a single Dirac cone on the surface. *Nat. Phys.* **5**, 398 (2009).
- Bianchi, M., Hatch, R. C., Mi, J., Iversen, B. B. & Hofmann, P. Simultaneous quantization of bulk conduction and valence states through adsorption of nonmagnetic impurities on Bi₂Se₃. *Phys. Rev. Lett.* **107**, 086802 (2011).
- Zangwill, A. *Physics at Surfaces* p. 21 (Cambridge Univ. Press, Cambridge, 1988).
- Feng, J. et al. Electronic structure and enhanced charge-density wave order of monolayer VSe₂. *Nano Lett.* **18**(7), 4493 (2018).
- Wang, Y. & Gedik, N. Circular dichroism in angle-resolved photoemission spectroscopy of topological insulators. *Phys. Stat. Solid.* **7**, 64–71 (2013).
- Scholz, M. R. et al. Reversal of the circular dichroism in angle-resolved photoemission from Bi₂Te₃. *Phys. Rev. Lett.* **110**, 216801 (2013).
- Miao, L. et al. Observation of a topological insulator Dirac cone reshaped by non-magnetic impurity resonance. *npj Quantum Mater.* **3**, 29 (2018).
- Schlénk, T. et al. Controllable magnetic doping of the surface state of a topological insulator. *Phys. Rev. Lett.* **110**, 126804 (2013).
- Yilmaz, T. et al. Photon energy and polarization-dependent electronic structure of Cr-doped Bi₂Se₃. *Phys. Rev. Mater.* **4**, 024201 (2020).
- Sánchez-Barriga, J. et al. Nonmagnetic band gap at the Dirac point of the magnetic topological insulator (Bi_{1-x}Mn_x)₂Se₃. *Nat. Commun.* **7**, 10559 (2016).
- Yilmaz, T. et al. Gap-like feature observed in the non-magnetic topological insulators. *J. Phys. Condens. Matter* **32**, 145503 (2020).
- Li, Z. et al. Realization of flat band with possible nontrivial topology in electronic Kagome lattice. *Sci. Adv.* **4**, eaau4511 (2018).
- Bianchi, M. et al. Coexistence of the topological state and a two-dimensional electron gas on the surface of Bi₂Se₃. *Nat. Commun.* **1**, 128 (2010).

Acknowledgements

This research used ESM (21-ID-1, 21-ID-2) beamline of the National Synchrotron Light Source II, a US Department of Energy (DOE) Office of Science User Facility operated for the DOE Office of Science by Brookhaven National Laboratory under Contract number DE-SC0012704. This work also used the resources of the Center for Functional Nanomaterials, Brookhaven National Laboratory, which is supported by the U.S. Department of Energy, Office of Basic Energy Sciences, under Contract number DE-SC0012704. ARPES experiments in Hiroshima were performed with the approval of program

advisory committee of HISOR) Proposal number 19BG041). T.Y. thanks Professor A.V. Balatsky for useful discussions.

Author contributions

T.Y. conceived and designed the experiments. T.Y. prepared the samples and performed the photoemission experiments with the help from K. Kaznatcheev, E.V., and B.S. E.F.S. and K.S. performed the ARPES experiments at HISOR. X.T. conducted the STM measurements. Z.D. and J.T.S. performed μ LEED measurements. S.H. and K. Kisslinger performed HAADF-STEM experiments. T.Y. analyzed the experimental results and wrote the manuscript with contribution from E.F.S., B.S., K. Kaznatcheev, and E.V.

Competing interests

The authors declare no competing interests.

Additional information

Supplementary information is available for this paper at <https://doi.org/10.1038/s43246-020-00115-w>.

Correspondence and requests for materials should be addressed to T.Y.

Peer review information Primary handling editor: John Plummer

Reprints and permission information is available at <http://www.nature.com/reprints>

Publisher's note Springer Nature remains neutral with regard to jurisdictional claims in published maps and institutional affiliations.



Open Access This article is licensed under a Creative Commons Attribution 4.0 International License, which permits use, sharing, adaptation, distribution and reproduction in any medium or format, as long as you give appropriate credit to the original author(s) and the source, provide a link to the Creative Commons license, and indicate if changes were made. The images or other third party material in this article are included in the article's Creative Commons license, unless indicated otherwise in a credit line to the material. If material is not included in the article's Creative Commons license and your intended use is not permitted by statutory regulation or exceeds the permitted use, you will need to obtain permission directly from the copyright holder. To view a copy of this license, visit <http://creativecommons.org/licenses/by/4.0/>.

© The Author(s) 2021